small
NANO MICRO
www.small-journal.com

Molten Salt Assisted Self-Assembly: Synthesis of Mesoporous $LiCoO_2$ and $LiMn_2O_4$ Thin Films and Investigation of Electrocatalytic Water Oxidation Performance of Lithium Cobaltate

Gülbahar Saat, Fadime Mert Balci, Elif Pınar Alsaç, Ferdi Karadas, and Ömer Dag**

Mesoporous thin films of transition metal lithiates (TML) belong to an important group of materials for the advancement of electrochemical systems. This study demonstrates a simple one pot method to synthesize the first examples of mesoporous $LiCoO_2$ and $LiMn_2O_4$ thin films. Molten salt assisted self-assembly can be used to establish an easy route to produce mesoporous TML thin films. The salts ($LiNO_3$ and $[Co(H_2O)_6](NO_3)_2$ or $[Mn(H_2O)_4](NO_3)_2$) and two surfactants (10-lauryl ether and cethyltrimethylammonium bromide (CTAB) or cethyltrimethylammonium nitrate (CTAN)) form stable liquid crystalline mesophases. The charged surfactant is needed for the assembly of the necessary amount of salt in the hydrophilic domains of the mesophase, which produces stable metal lithiate pore-walls upon calcination.
The films have a large pore size with a high surface area that can be increased up to 82 $m^2 g^{-1}$. The method described can be adopted to synthesize other metal oxides and metal lithiates. The mesoporous thin films of $LiCoO_2$ show promising performance as water oxidation catalysts under pH 7 and 14 conditions. The electrodes, prepared using CTAN as the cosurfactant, display the lowest overpotentials in the literature among other $LiCoO_2$ systems, as low as 376 mV at 10 mA cm^{-2} and 282 mV at 1 mA cm^{-2}.

1. Introduction

Nanostructured, self-assembled metal oxides represent an important group of materials that may advance material demanding technologies, such as catalysis, clean energy generation, and storage.[1–5] Recently, it has been shown that the nanostructured lithium cobaltate ($LiCoO_2$) is a good candidate for use as a water-oxidation catalyst.[4,5] However, in reviewing the literature, the synthesis of mesoporous metal oxides and metal lithiates has always been a challenge. Many strategies for synthesis, including hard and soft templating methods, have been developed over the years.[6–20] The lyotropic liquid crystalline (LLC) templating method has also been employed to produce metals and metal oxides with the help of a reducing agent or electrochemical methods.[21–25]

Unfortunately, the many existing metal ion precursors are not appropriate for use in soft and hard templating. There are some successful examples of the synthesis of mesoporous metal oxides by using alkoxy precursors.[26–30] However, most metal precursors are common ion salts, such as metal chlorides, nitrates, sulfates, and acetates, that need high temperatures to undergo hydrolysis and condensation reactions to form their oxides. Even if one can incorporate the salts into mesophases, in the next step, in going from salt precursors to oxides, the salt species shrink by 70–90%, which causes a collapse of the meso-order in soft templating processes or a nonuniform coating in the hard-templating cases.[6–20] There are no examples of mesoporous thin films produced through hard-templating and there has been limited success with soft templating methods. In particular, the oxides that contain two or more metals are even more difficult to assemble into mesoporous materials. It is still extremely challenging to form and maintain mesostructures in most metal based materials.

Although, there are some successful examples of mesoporous metal lithiates powders, using hard templating method,[15–20] the method is quite complex and generally impossible to produce thin films. Bruce and co-workers reported the first synthesis of mesoporous low temperature spinel $LiCoO_2$ and $LiCoO_2$ nanowires.[31] The synthesis of mesoporous spinel $LiMn_2O_4$ has been reported by Luo et al.[32] Hwang et al. obtained the mesoporous metal lithiates by using soft templating.[33] The resulting material had a 3.8 nm pore size, 31 nm wall thickness, and 13.8 $m^2 g^{-1}$ surface area.[34] Chen et al. used P123, $Mn(CH_3COO)_2.4H_2O$, and $LiOH.H_2O$ as ingredients to produce $LiMn_2O_4$ with a pore size of 5.5 nm and a surface area of 42.5 $m^2 g^{-1}$.[35] However materials with a larger surface area,

G. Saat, Dr. F. M. Balci, E. P. Alsaç, Prof. F. Karadas, Prof. Ö. Dag
Department of Chemistry
Bilkent University
06800 Ankara, Turkey
E-mail: karadas@fen.bilkent.edu.tr; dag@fen.bilkent.edu.tr
Prof. F. Karadas, Prof. Ö. Dag
UNAM-National Nanotechnology Research Center and Institute of Materials Science and Nanotechnology
Bilkent University
06800 Ankara, Turkey
The ORCID identification number(s) for the author(s) of this article can be found under https://doi.org/10.1002/smll.201701913.

DOI: 10.1002/smll.201701913

thinner pore-walls, and larger pore sizes are in demand for the use of these materials in electrochemical devices.[31–37]

Molten salt-assisted self-assembly (MASA) is an important synthesis process used to fabricate mesoporous transparent thin films of metal oxides.[38–41] The method has been first employed to produce mesoporous CdO and ZnO coated silica, where the CdO and ZnO can be homogeneously coated over silica pore-walls as thin as 1.6 nm.[38] Later, many mesoporous metal titanates ($CdTiO_3$, Zn_2TiO_4, $CoTiO_3$, $MnTiO_3$, and $Li_4Ti_5O_{12}$) have been synthesized using the MASA method.[39–41] In this process, both ethanol (or water in some cases) and the salt species act as two different solvents to dissolve and to assemble surfactants into the mesophases, respectively. A silica or titania source is added to the media, where their polymerization starts in the solution phase and enhances with coating to form the gel phase. During the process, two surfactants (charged and neutral) are also required to form stable mesophases with high salt concentrations.[38–41] Mesoporous materials prepared, up to now, using the MASA process have always been carried out in the presence of a polymerizing agent (metal alkoxides).[38–41]

Many salts and nonionic surfactants with/without a charged surfactant form stable LLC mesophases.[42–44] Notice that the salt surfactant mesophases are stable phases and do not undergo any solidification process at room temperature and are mostly stable up to their melting points.[42–44] Therefore, it is still a challenge in the current literature to form stable mesostructures of many metal salts that can be converted into a mesoporous material upon calcination without a polymerizing reagent in the media.

Here, for the first time, we applied the MASA process to nonpolymerizing salts to obtain metal lithiate (such as $LiCoO_2$ and $LiMn_2O_4$) thin films that may find application for various electrochemical processes.

2. Results and Discussion

2.1. Synthesis and Characterization of Mesoporous $LiCoO_2$ Thin Films

The first step in the synthesis is to prepare a clear homogeneous solution of the ingredients (salts, surfactants, ethanol or water, acid). One must make sure that all the salts are completely dissolved in the solution; otherwise they crystallize very quickly when coated over a substrate. Coating (spin, dip, or spray coatings) of the clear solutions produces transparent LLC films in a short time. The freshly prepared films diffract at small angles and are birefringent under polarized optical microscopy (POM). Both lithium and metal nitrate salts, separately and/or together, form stable LLC mesophases. **Figure 1** shows a set of small angle X-ray diffraction (XRD) patterns of the $LiNO_3$-$[Co(H_2O)_6](NO_3)_2$-$C_{12}E_{10}$-cethyltrimethylammonium bromide (CTAB) ($C_{12}E_{10}$ stands for $C_{12}H_{25}(OCH_2CH_2)_{10}OH$, 10-lauryl ether) samples with a different salt content. The sample number (sample #), throughout the text, is the total salts (quantitative among $LiNO_3$ + $[Co(H_2O)_6](NO_3)_2$ with a 1:1 mole ratio) to $C_{12}E_{10}$ mole ratio. The $C_{12}E_{10}$/CTAB ratio is one and kept constant in all samples. The diffraction line, observed at around 2.13°, shifts to 1.35°, corresponding to 46 to 72.6 Å d-spacing, by increasing salt/surfactant ratio from 4.5 to 15, respectively, see Figure 1. The sample-16 also broadly diffracts at around 1.25°, 2θ, but above this ratio, it is completely disordered, in that the mixture leaches out salt crystals. The coated samples are birefringent up to 9 salt/$C_{12}E_{10}$ mole ratio and display focal conic fan texture between the crossed polarizers under POM, see Figure S1 (Supporting Information). Therefore, it is likely that the mesophase is 2D hexagonal up to a mole ratio of 9 and becomes cubic above this ratio.[42–44] Note also that the $LiNO_3$-$C_{12}E_{10}$ is hexagonal up to a mole ratio of 8 and $[Co(H_2O)_6](NO_3)_2$-$C_{12}E_{10}$ is up to 3.2 without CTAB. The presence of CTAB and the synergic effects of two salts in the media enhance the hexagonal region up to mole ratios of 9 and the cubic phase to up to mole ratios of 16 in the mesophase in two salts two surfactant systems.[42–44]

The hydrophobic forces among the alkyl tails and hydrogen bonding and ion-dipole network among the hydrophilic domains of the surfactant molecules and salt species hold the micelle units of the mesophase together, up to a 16 salt/surfactant mole ratio. Also noticed from the solution composition that around 75% of the mesophase composition is salt. This ratio is the highest ever seen in salt-surfactant mesophases and is important for the synthesis of porous materials, since the pore walls will be constructed from these metal species.

To determine whether there were any salt crystals, leached out of the mesophase, the wide angle XRD patterns of the samples were also measured from the aged samples; see Figure 1b. The wide angle XRD patterns of the aged samples exhibited no diffraction lines, indicating no salt or CTAB crystallization, even after 60 min of aging the films. The mesophases, in all compositions, were stable over the required period and were ready for further heat treatments. It also indicates that the salt species are in the molten state in the hydrophilic domain of the mesophases.[45]

Many parameters, such as the volatile solvent, amount of salt, presence of CTAB or cethyltrimethylammonium nitrate (CTAN), calcination temperature, etc., were systematically investigated using both fresh mesophases and their calcination products. The role of the volatile solvent has been investigated using water and ethanol. The clear solutions of the ingredients were prepared separately in both solvents, with and without CTAB, and spin coated over silicon wafers and glass slides to collect their Raman spectra and XRD patterns upon calcination, respectively, see **Figure 2**. The calcined samples are denoted as meso-$LiCoO_2$-# (# is again the total salt/$C_{12}E_{10}$ mole ratio).

The Raman spectra of two sets of calcined samples are shown in Figure 2. Note that $LiCoO_2$ has two common phases, one with a hexagonal symmetry that has two Raman active modes at 486 and 597 cm^{-1}, arising from the E_g and A_{1g} modes, respectively.[46–48] The other $LiCoO_2$ phase has a spinel structure and exhibits peaks at 483, 525, 621, and 690 cm^{-1} that correspond to the $2T_g$, E_g, and A_{1g} modes, respectively.[46–48] The spinel Co_3O_4 has also five Raman modes at 194, 488, 522, 618, and 691 cm^{-1}.[46–48] The sample, prepared using the water solution, has distinct Co_3O_4 peaks at 194 and 691 cm^{-1} and the sample, prepared using the ethanol solution has relatively stronger peaks of $LiCoO_2$ at 486 and 597 cm^{-1}, Figure 2a,b. The peak at 522 cm^{-1} is likely due to Si wafer and T_{2g} mode of Co_3O_4.

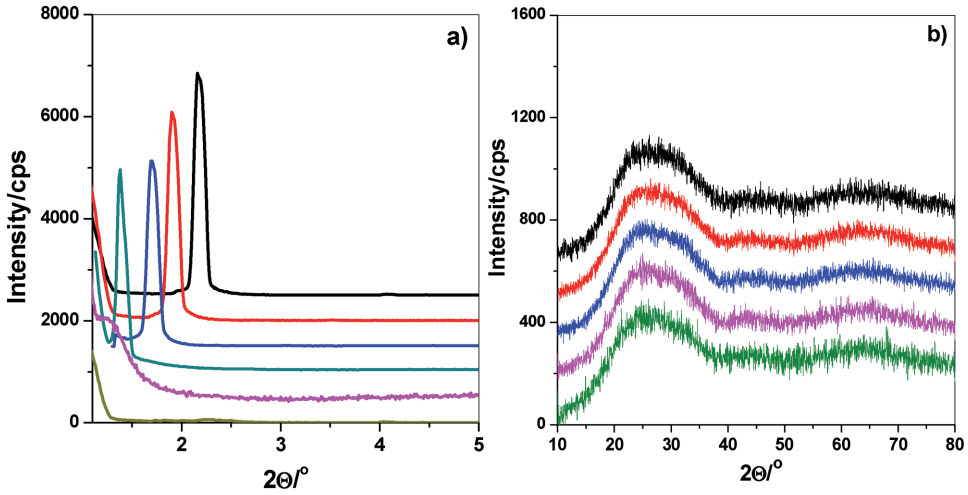

Figure 1. XRD patterns of fresh thin films of $LiNO_3$-$[Co(H_2O)_6](NO_3)_2$-$C_{12}E_{10}$. a) Small angle and b) wide angle regions upon 60 min aging (top to bottom, salts/surfactant mole ratio of 4.5, 9, 12, 15, 16, and 17).

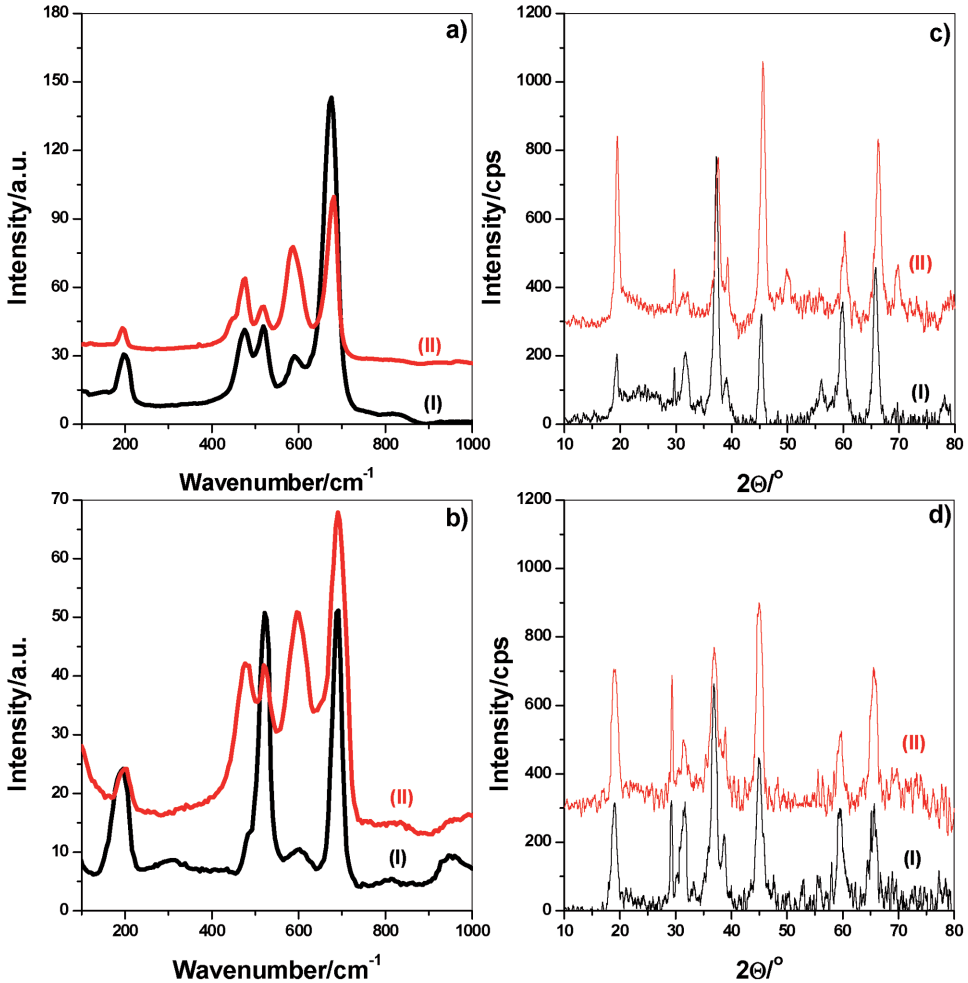

Figure 2. Raman spectra of the calcined sample of meso-$LiCoO_2$-9 a) without CTAB and b) with CTAB, prepared in (I) water and (II) ethanol. c,d) XRD pattern of the same samples in panels (a) and (b).

The XRD patterns of the same samples also confirm the Raman data, Figure 2c,d. The XRD pattern predominantly consists of diffraction lines of low temperature (LT) $LiCoO_2$ and Co_3O_4 or partially lithiated $Li_{1-x}CoO_2$. The formation of meso-$LiCoO_2$ is enhanced if the process is initiated in an ethanol solution. Unfortunately, the diffraction patterns of Co_3O_4 and $LiCoO_2$ are very similar with the most intense line at 45.4° in the $LiCoO_2$ and at 37.3° in the Co_3O_4 with a distant line at around 29.5°, 2θ. Overall, if one examines the intensity of these two lines, the intensity ratio alters going from ethanol to water media. Both Raman spectra and XRD patterns collectively show that the $LiCoO_2$ forms more in the samples obtained using ethanol and therefore ethanol is a better solvent to synthesize the meso-$LiCoO_2$.

To optimize the salt concentration, another set of samples were prepared using ethanol as the solvent, by changing the amount of salt in the mesophase. The meso-$LiCoO_2$-# (# is 4.5, 6, 9, 12, 15, and 16, respectively) films were prepared by calcining the freshly coated films (from the corresponding clear ethanol solutions) at 450 °C to elucidate the role of salt amounts in the mesophase and the calcined final products. The powders, collected by scraping from around 60 glass slides were used to collect the XRD patterns and N_2 sorption isotherms. The diffraction patterns of the above samples displayed very similar XRD patterns with few differences. The N_2 sorption isotherms display type IV isotherms in all compositions with a hysteresis, indicating the mesoporous nature of the samples, **Figure 3**. The Barrett–Joyner–Halenda (BJH) pore size distribution plots of the desorption branches displayed a relatively more uniform pore in the meso-$LiCoO_2$-4.5 to meso-$LiCoO_2$-9 samples; nonuniform and larger pores are observed in the samples with higher salt content, compare pore size plots in Figure 3. The N_2 sorption isotherms have also been collected from the meso-$LiCoO_2$-9 samples, prepared with and without CTAB in the mesophase to elucidate the role of CTAB. It is shown that the sample having no CTAB has a nonuniform pore size distribution and a lowest surface area.

Note that a charge surfactant, CTAB, is necessary for the synthesis of stable porous metal oxides with a more uniform pore size distribution and for the assembly of a large amount of salts, however it also causes problems. For instance, the addition of CTAB in the clear solutions of Co(II) changes the color of the solution from dark pink to dark blue. The origin of the blue color is the $[CoBr_4]^{2-}$ complex ion in ethanol solution and it prompts the formation of the $(CTA)_2[CoBr_4]$ complex salt, which has a low solubility and causes problems during decomposition at higher temperatures. To analyze the effect of Br^- ion on the formation of side products, the solutions prepared with/without CTAB have been spectroscopically

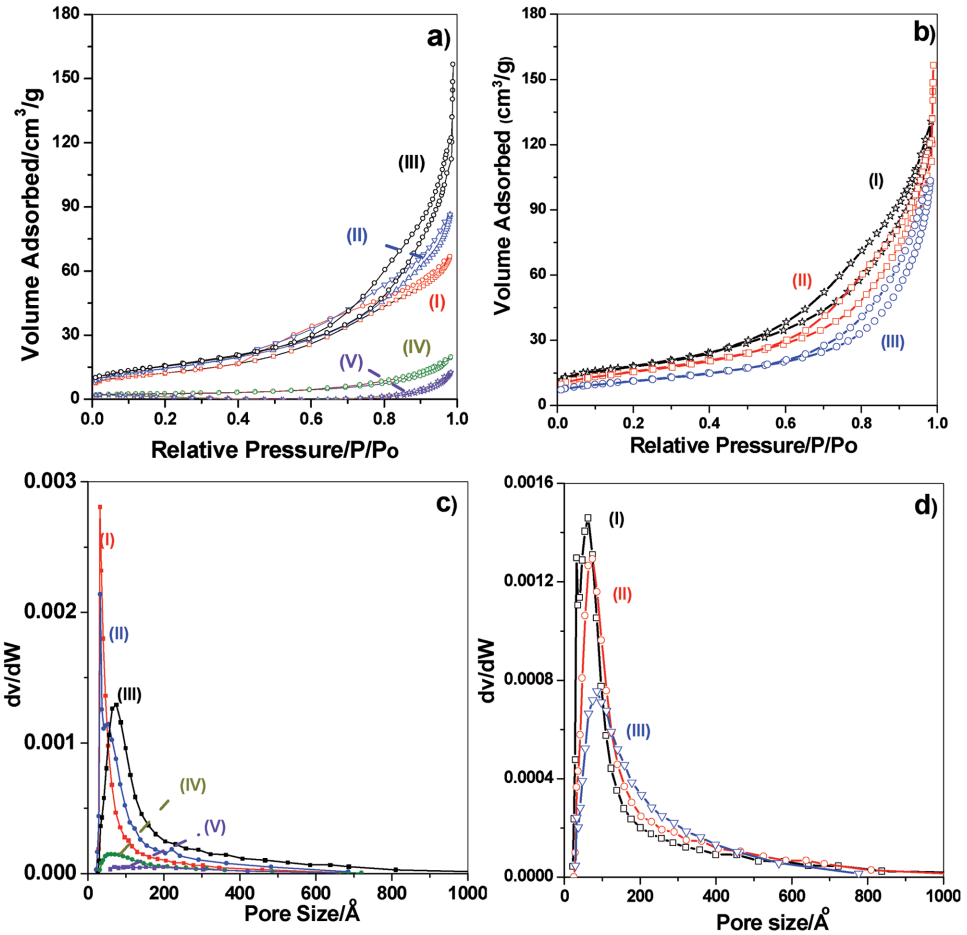

Figure 3. N_2 sorption isotherms a) of meso-$LiCoO_2$-#, # is (I) 4.5, (II) 6, (III) 9, (IV) 12, and (V) 15, and b) of meso-$LiCoO_2$-9, calcined at (I) 300, (II) 450, and (III) 550 °C. c,d) BJH pore size distribution plots of the same samples in panels (a) and (b), respectively.

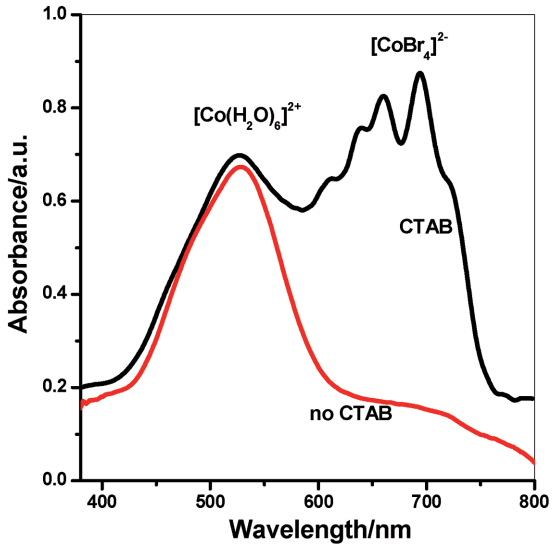

Figure 4. UV–vis spectra of the fresh samples prepared with/without CTAB as labeled.

examined, see **Figure 4**. A broad absorption band at 532 nm is observed in both samples, due to the presence of $[Co(H_2O)_6]^{2+}$ ion, but in the sample containing CTAB, there are also fingerprint absorption bands of tetrahedral $[CoBr_4]^{2-}$ ion,[49] the absorption between 550 and 750 nm, indicating the formation of $(CTA)_2[CoBr_4]$ complex surfactant salt, Figure 4.

To further elucidate the role of Br^- ion in the media, cobalt nitrate was partially replaced with $CoBr_2$ (2.5 cobalt nitrate + 2 cobalt bromide) to increase the Br^- ion concentration in the media and a set of samples using a 9 salt/surfactant mole ratio was prepared and calcined at 400 °C for 3 h. **Figure 5** shows

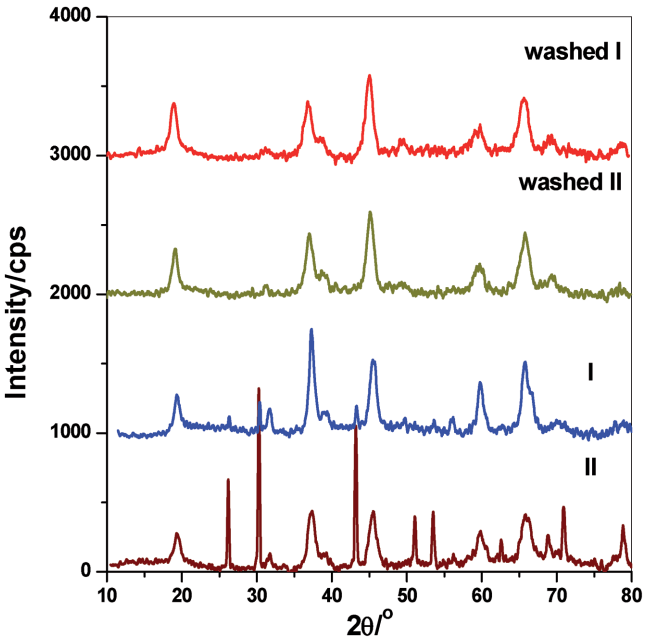

Figure 5. The XRD pattern of the powders, with and without washing, of (I) $[Co(H_2O)_6](NO_3)_2$ only cobalt source and (II) two cobalt source ($CoBr_2$ + $[Co(H_2O)_6](NO_3)_2$).

a set of the XRD pattern of those samples. The patterns were simultaneously collected upon calcination and then after washing the calcined sample with distilled water. It is shown that the addition of $CoBr_2$ enhanced the intensity of sharp lines and some new lines appeared in the patterns, due to impurities in the samples. However, upon washing the samples, the sharp lines disappeared, indicating that some of the side products are unreacted salt species, see Figure 5; washing leaves only the insoluble Co_3O_4 and $LiCoO_2$ signals in the patterns. Note also that the $CoBr_2$ crystals are stable under air even at 700 °C. Therefore, the crystallization and phase separation of the $(CTA)_2[CoBr_4]$ complex salt that decomposes into $CoBr_2$ and other oxides, CoO and Co_3O_4 are the origin of the impurities. However, the CTAB free samples also produce Co_3O_4 nanocrystallites. While the source of the impurities is $(CTA)_2[CoBr_4]$ complex crystals in the presence of CTAB, in the absence of CTAB, it is the cobalt nitrate salt crystal that is leached out from the mesophase at such high salt concentrations. In other words, the charged surfactant is necessary to accommodate salt species in their molten phase in the mesophase at high salt concentrations; otherwise the excess salt is leached out from the media as salt crystals to form the bulk oxides at elevated temperatures during the calcination process.

To overcome the negative effect of Br^- ion, a new surfactant (CTAN) has been synthesized by exchanging Br^- ion with NO_3^- ion as described in the experimental part. Both Fourier transform infrared (FT-IR) spectrum and XRD pattern of CTAN clearly show that the exchange process is quite effective; the absorption peak of NO_3^- at around 1324 cm^{-1} is distinctively observed and the XRD patterns of CTAB and CTAN display very similar diffraction patterns with a slight change on the line positions, indicating that they have a similar crystal structure, Figure S2 (Supporting Information).

A set of samples were prepared using CTAN in place of CTAB to identify the side products. **Figure 6** displays two POM images, characteristic of a 2D hexagonal phase, from the fresh and calcined film of 6 salt/$C_{12}E_{10}$ mole ratio, prepared using CTAN, Figure 6a,b. The sample prepared using CTAN shows only the lines from pure $LiCoO_2$, see Figure 6c. The data clearly show that the separation of the salt (as of cobalt nitrate or $(CTA)_2[CoBr_4]$) produces the side products. Therefore, the process requires a charged surfactant which cannot form a complex with the salt. These samples were further investigated at higher temperatures by collecting their XRD and N_2 sorption isotherms. The results of the isotherms are tabulated, considering all the parameters, in **Table 1** for comparison. Clearly the pores get larger by increasing the calcination temperature at the expense of a smaller surface area and pore volume due to crystallization and growth on the pore walls.

The transmission electron microscope (TEM) and scanning transmission electron microscope (STEM) images of meso-$LiCoO_2$-9 (calcined at 450 °C for 1 h) are shown in **Figure 7**. The highly crystalline structure of the $LiCoO_2$ is clearly visible in the images. The size of the crystalline domains varies from 3 to 10 nm. The STEM image shows a piece of meso-$LiCoO_2$-9 film with homogeneous mesopores in the film. Further analysis of the HR-TEM image shows that the lattice fringes due to (003) planes of $LiCoO_2$ with a d-spacing of 0.468 nm (consistent with the XRD results) are clearly visible throughout the

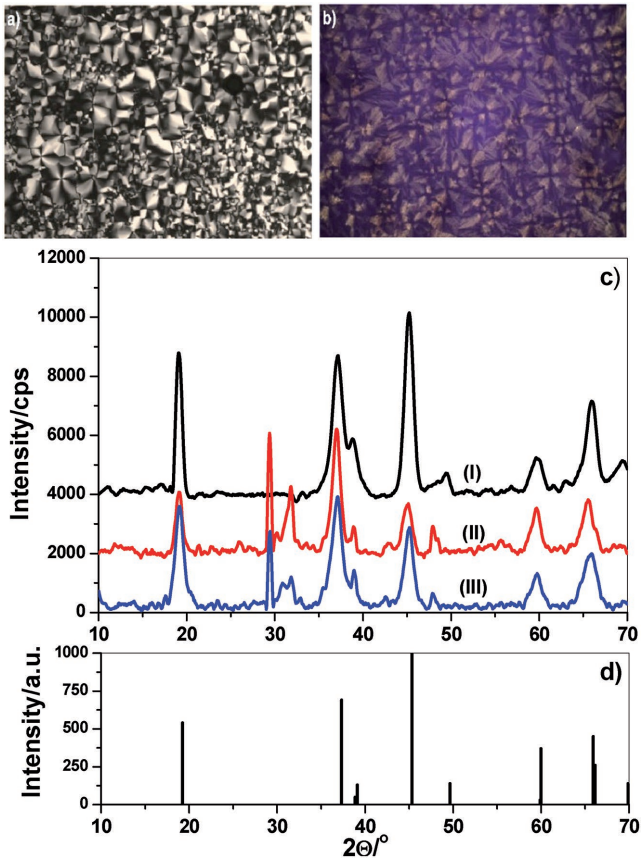

Figure 6. The POM images of a) fresh film and b) calcined film of the sample prepared using CTAN of meso-$LiCoO_2$-6 system and c) the XRD patterns of meso-$LiCoO_2$-6 prepared using (I) CTAN, (II) CTAB, and (III) no charged surfactant, and d) Powder Diffraction File (PDF) card (JCPDS 044-0145).

image, see Figure S3 (Supporting Information). Notice also that the $LiCoO_2$ nanocrystallites are mainly oriented along the *c*-axis of nanocrystallites, making the pore-walls. However, further imaging with higher resolution may require identifying the other planes of the $LiCoO_2$ pore-walls.

Table 1. N_2 sorption data of selected samples (CT = calcination temperature, BET = Brunauer–Emmett–Teller, SA = surface area, PS = pore size, and PV = pore volume).

Samples	CT [°C]	BET SA [$m^2\ g^{-1}$]	BJH PS [nm]	PV [$cm^3\ g^{-1}$]
Meso-$LiCoO_2$-9	300	60	10	0.24
Meso-$LiCoO_2$-9	450	56	15	0.20
Meso-$LiCoO_2$-9	550	41	16	0.16
Meso-$LiCoO_2$-4.5	450	40	7	0.13
Meso-$LiCoO_2$-6	450	45	8	0.11
Meso-$LiCoO_2$-9*[a)]	450	65	15	0.22
Meso-$LiCoO_2$-9*[b)]	350	58	11	0.18
Meso-$LiCoO_2$-9*[b)]	400	46	13	0.15
Meso-$LiCoO_2$-9*[b)]	450	34	16	0.12

*Prepared using CTAN and annealed for [a)]1 h and [b)]10 h.

2.2. Synthesis and Characterization of Mesoporous $LiMn_2O_4$ Thin Films

The same procedure and optimization parameters, used in the $LiCoO_2$, were also employed in the synthesis of mesoporous $LiMn_2O_4$ films, denoted as meso-$LiMn_2O_4$-# (# is the total salt/$C_{12}E_{10}$ mole ratio). The major difference between the Co(II) and Mn(II) systems is the total salt/surfactant mole ratio (2Mn(II) for each Li(I)) and the effect of the acid used in the $LiCoO_2$ system. Like the Co(II) system, the mesophase is ordered and the unit cell expansion is also clearly visible with increasing salt content (up to 12 salt/surfactant mole ratio) in the fresh films, see Figure S4 (Supporting Information). Notice that the transition metal salt concentration is the determining parameter for the salt limits in the stable mesophases; the highest transition metal salt, in both systems, are the same (8 Mn(II) in 12 salts in the Mn(II) system and 8 Co(II) in 16 salts in the Co(II) system).

Figure S4a (Supporting Information) shows a set of XRD patterns and POM images of the fresh samples of $LiNO_3$-$[Mn(H_2O)_4](NO_3)_2$-$C_{12}E_{10}$-CTAB samples with four different salt/surfactant mole ratios. The diffraction patterns of the fresh samples up to 12 salts (8 Mn(II) + 4 Li(I))/$C_{12}E_{10}$ mole ratio display intense diffraction lines at small angles. The POM images of the fresh samples, shown in Figure S4b (Supporting Information) are also consistent with the XRD data and display fan like texture under POM up to 12 salt/surfactant mole ratio.

The role of the volatile solvent has also been investigated in the Mn(II) system as well, using both ethanol and water. The mixture, prepared using ethanol is a clear yellow solution. However, the mixture prepared using water yields a yellow precipitate with the addition of $[Mn(H_2O)_4](NO_3)_2$ salt to the media which did not dissolve again after 1 week of stirring. The yellow precipitate was also collected and analyzed using XRD, see Figure S5 (Supporting Information). The diffraction pattern clearly shows the yellow product containing charged surfactant and Mn(II) complex ion; it is likely that the $(CTA)_2[MnBr_4]$ crystallites like its cobalt analog. Because a clear solution was obtained using ethanol, it was used as the solvent for further experimentation.

Different from the Co(II) system, the Mn(II) system needed an acidic media to stabilize the Mn(II) species in the solution and LLC mesophases. The Mn(II) species likely undergoes oxidation that leads to hydrolysis and condensation reactions to form brown powders of manganese oxides/hydroxides species. The addition of acid halts the side reactions and stabilizes the Mn(II) in the solution and in the mesophase upon coating the clear solution, composed of all ingredients. The films were calcined at various temperatures and durations and analyzed using FT-IR, Raman, XRD, N_2 sorption, and TEM techniques.

The calcination process was monitored using FT-IR spectroscopy, see Figure S6 (Supporting Information). The two absorption bands, observed at 518 and 617 cm^{-1} become clear at around 160 °C; these two peaks have been assigned to cubic nano-$LiMn_2O_4$ spinel in the literature.[48,50] However, the peaks of nitrate, water, and surfactants completely disappear at around 300 °C, Figure S7 (Supporting Information). Therefore, the minimum calcination temperature for the synthesis has been determined to be 300 °C for the meso-$LiMn_2O_4$ samples, however the formation of $LiMn_2O_4$ begins at temperatures

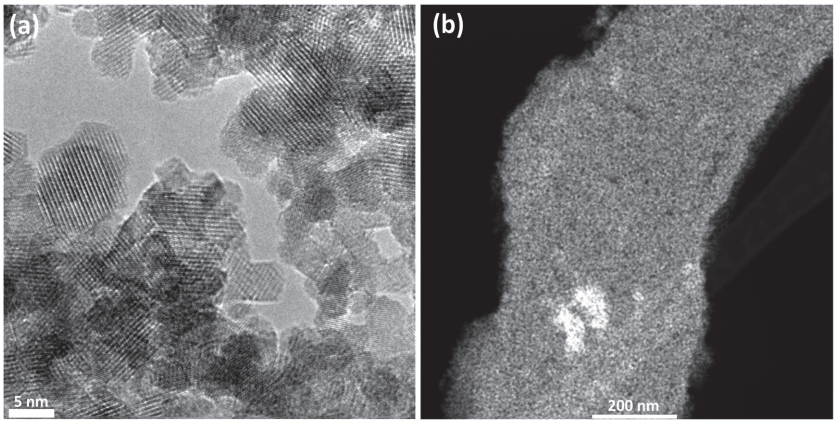

Figure 7. a) TEM (left) and b) STEM (right) images of meso-$LiCoO_2$-9.

as low as 160 °C. To set the duration and verify the temperature, the sample of meso-$LiMn_2O_4$-9 was calcined 3 times at 300 °C for 1 h durations and the XRD patterns of the sample were recorded after each calcination step, **Figure 8**a. As it is shown in Figure 8, the XRD patterns of the sample, calcined for 1 and 2 h, there appears a line around 29.2°, which does not belong to $LiMn_2O_4$ and which completely disappears after 3 h of calcination.

The effect of Br^- ion was also checked in the Mn(II) system, where both CTAN and CTAB have been used as the charged surfactant in the assembly process. While a yellow solution forms in the presence of CTAB, the solutions in the case of CTAN was clear with a very light pink color due to the Mn(II) species, see Figure S6 (Supporting Information). Both solutions have been spin coated over a substrate and calcined at 300 °C for 12 h to determine if there are any side products that might form large crystals and become visible in the XRD pattern over longer durations. As shown in Figure 8c; there are no differences between the patterns of the samples prepared using CTAB versus CTAN as the charged surfactant; the process produces mesoporous $LiMn_2O_4$ with nanocrystalline pore-walls. The Raman spectra of the samples also confirm the XRD results; compare the spectra and pattern in Figure S8 (Supporting Information). The most intense Raman band, located at around 625 cm^{-1}, is attributed to the symmetric stretching vibration of the MnO_6 units and there also exists a group of bands between 200 and 500 cm^{-1} with a weaker intensity.[48] Both samples have similar Raman spectra, indicating that none of the samples produce any side products.

The role of the salt content in the mesophase has also been investigated in the synthesis of mesoporous $LiMn_2O_4$. For this purpose, the wide angle XRD patterns, Raman spectra, and N_2 sorption isotherms of the samples, prepared using 4.5, 6, 9, 12, and 14 (Li(I) + Mn(II))/$C_{12}E_{10}$ mole ratios were also recorded, see Figure S9 (Supporting Information). The XRD patterns of the samples, calcined at 300 °C for 3 h, displayed neither visible change in intensities of the diffraction lines nor extra lines due to side products in all compositions, see Figure S9a (Supporting Information). The Raman spectra of the samples also confirm the XRD data. As shown in Figure S8b (Supporting Information); with increasing salt quantities in the mesophase, the peaks located at 625 cm^{-1} and the other weaker ones (all belong to $LiMn_2O_4$) slightly broaden around their location, which is attributed to the nanocrystalline nature of the $LiMn_2O_4$ pore-walls and there is no sign of any side products. The N_2 sorption data were also collected from the same samples, Figure S9c,d (Supporting Information). The isotherms are type IV and display hysteresis, characteristic for the mesoporous materials. The specific surface area of the samples is also calculated as of 55, 66, 71, and 82 $m^2\ g^{-1}$ from the samples obtained from 4.5, 6, 9, and 12 salt ratios, respectively. The pore size distribution of the samples is also shown in Figure S9b (Supporting Information). The BJH desorption pore sizes are 7, 9, 11, and 11 nm and the pore volumes of 0.15, 0.16, 0.24, 0.29 $cm^3\ g^{-1}$

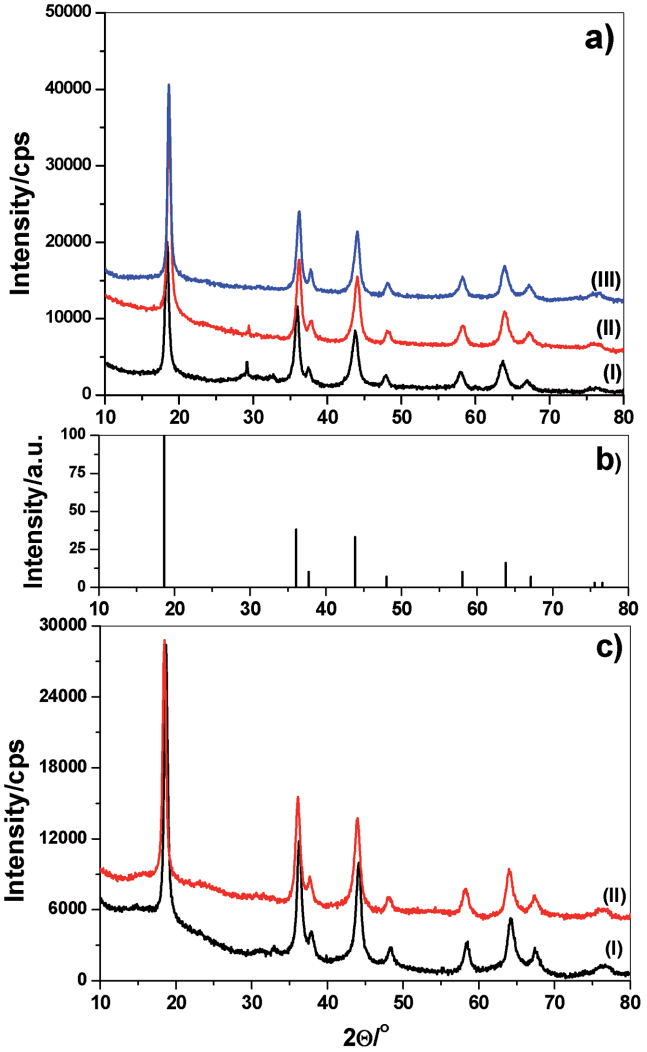

Figure 8. XRD patterns of the powder of a) meso-$LiMn_2O_4$-9, calcined at 300 °C for a duration of (I) 1, (II) 2, and (III) 3 h. b) The PDF card (JCPDS 035-0782) of $LiMn_2O_4$ and c) meso-$LiMn_2O_4$-6, from (I) CTAB and (II) CTAN, calcined at 300 °C for 12 h.

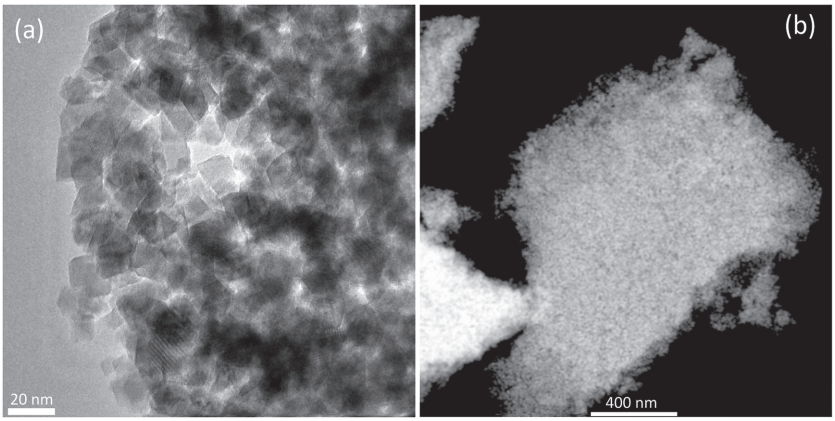

Figure 9. a) TEM image and b) STEM image of meso-$LiMn_2O_4$.

in the same samples. However, the pore size is more uniform at lower salt compositions.

The TEM and STEM images of the mesoporous $LiMn_2O_4$ thin films are shown in **Figure 9**. A sponge like mesoporous $LiMn_2O_4$ thin films form with highly crystalline pore walls (10–15 nm), see Figure 9, like the meso-$LiCoO_2$ films.

2.3. Electrocatalysis of Meso-$LiCoO_2$ Thin Films for Water Oxidation

Meso-$LiCoO_2$-9 samples were further investigated for use in water oxidation. The electrochemical studies were performed on a series of meso-$LiCoO_2$-9@FTO electrodes, which were prepared by using CTAN and CTAB as the charge surfactants and at different calcination temperatures to investigate the effect of the charged surfactant and annealing temperature to the electrocatalytic performance. Cyclic voltammograms (CVs) of all the CTAB and CTAN samples exhibit similar profiles at pH 7 with a quasi-reversible redox process at around 1.6 V vs reference hydrogen electrode (RHE) (assigned to $Co^{3+/4+}$ redox process), which is followed by a significant increase in current density due to electrocatalytic water oxidation process (Figure S10, Supporting Information). A similar trend with an enhanced onset potential (≈1.4 V) was obtained at pH 14 (Figure S10, Supporting Information). The best performing samples of meso-$LiCoO_2$ from each surfactant, CTAB-450 (denoted as meso-$LiCoO_2$-I) and CTAN-400 (denoted as meso-$LiCoO_2$-II), prepared using CTAB and CTAN as charged surfactants and calcined at indicated temperatures, respectively, have been selected for further investigation. The cyclic voltammograms of meso-$LiCoO_2$-I and meso-$LiCoO_2$-II at pH 14 are displayed in **Figure 10**. The CVs indicate that the meso-$LiCoO_2$-II exhibits an onset potential of ≈1.35 V that is lower than that of meso-$LiCoO_2$-I (≈1.50 V) and both are also lower than the previously reported $LiCoO_2$ electrodes, which were prepared using a porous polymer precursor approach (≈1.52 V) and sol–gel procedure (≈1.60 V).[51–53] A CV measurement with $LiCoO_2$, which was prepared with nonionic surfactants, has also been performed at pH 14. A comparison of CVs obtained for meso-$LiCoO_2$-I, meso-$LiCoO_2$-II, and the one derived from nonionic surfactant (denoted as meso-$LiCoO_2$-III) clearly shows the effect of charged surfactant to the electrochemical properties, see Figure S12 (Supporting Information). The likely reason for a lower onset potential and better catalytic activity for meso-$LiCoO_2$-II could be better purity, higher surface area, and full mesoporosity throughout the films.

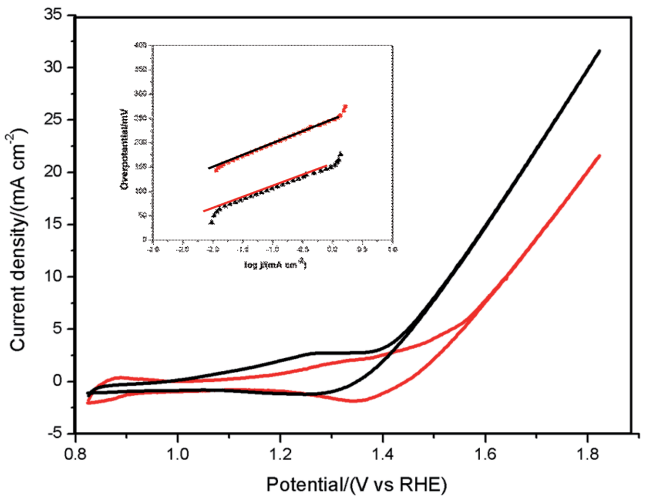

Figure 10. Cyclic voltammograms of meso-$LiCoO_2$-I (red line, upper curve) and meso-$LiCoO_2$-II (black line, upper curve) at pH 14. Inset: Tafel slopes.

Meso-$LiCoO_2$-I and meso-$LiCoO_2$-II samples exhibit Tafel slopes of 51 and 49 mV dec^{-1}, respectively, at pH 14, which are characteristic of a catalytic water oxidation mechanism involving a reversible one-electron transfer followed by a chemical process. The Tafel slopes increase moving from a high to a low pH, see Figure S13 (Supporting Information). The upper bound turnover frequencies (TOFs) were estimated using the BET surface areas of samples assuming a 100% Faradaic efficiency and that all atoms on the surface are active. The TOFs of meso-$LiCoO_2$-I and meso-$LiCoO_2$-II are calculated to be 44 and 42 s^{-1} cm^{-2}, respectively, at pH 14 and at $j = 10$ mA cm^{-2}, which are comparable to those obtained for the cubic Co_3O_4 nanocrystals[54] (**Table 2**).

Chronopotentiometric measurements have also been carried out under neutral (pH 7) and basic conditions (pH 14) to evaluate their electrocatalytic performances. A 21 h experiment was performed at $j = 1$ mA cm^{-2} followed by a 2 h one at $j = 10$ mA cm^{-2}, see **Figure 11**. The overpotential reaches a

Table 2. Summary of OER activities.

Meso-$LiCoO_2$-9*	TOF [s^{-1} cm^{-2}]	pH	Tafel slope	η for 1 mA cm^{-2}	η for 10 mA cm^{-2}
CTAB-450[a)]	44	14	51	340	426
	4.6	7	83	468	832
CTAN-400[b)]	42	14	49	282	376
	3.8	7	86	319	544

*BET surface area of [a)]55 and [b)]62 m^2 g^{-1}.

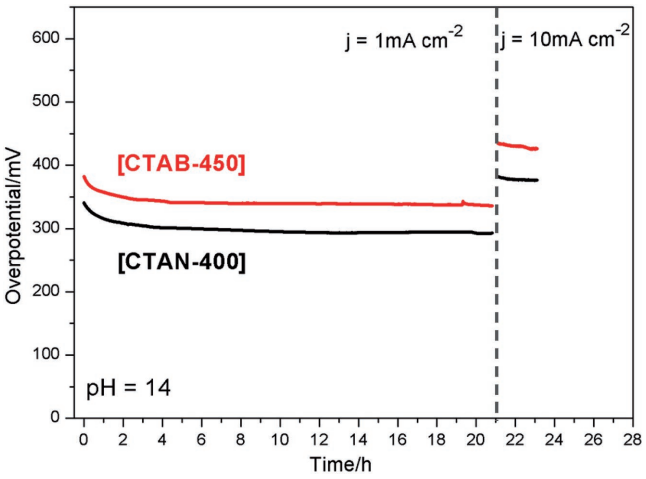

Figure 11. Chronopotentiometry experiment performed on meso-$LiCoO_2$-I (red line, upper) and meso-$LiCoO_2$-II (black line, lower) electrodes at j = 10 mA cm^{-2} for 21 h followed by a 2 h experiment at j = 10 mA cm^{-2}.

steady-state after an activation process, which takes around 3 h for both electrodes in the 1 mA cm^{-2} experiment and reaches an overpotential of 282 and 340 mV at pH 14 for the meso-$LiCoO_2$-II and meso-$LiCoO_2$-I, respectively. At j = 10 mA cm^{-2}, the electrodes maintain a stable overpotential at 376 and 426 mV for meso-$LiCoO_2$-II and meso-$LiCoO_2$-I, respectively, which are slightly lower than those previously reported in the $LiCoO_2$ systems. A similar trend at higher overpotentials was also observed at pH 7, see Figure S14 (Supporting Information). The chronopotentiometry experiments performed at different pH media and at different current densities suggest high stability and durability of each catalysts, which may be attributed to the strong attachment of the meso-$LiCoO_2$ films to the electrode surface, due to the novel in situ preparation method. The slightly better performance of the electrodes, prepared using CTAN can be attributed to a slightly higher surface area and fewer impurities in the CTAN derivative. Given the nature of the assembly process, it should be noted that there is still room for the optimization of the film quality and surface properties of meso-$LiCoO_2$ films for further improvement in the electrocatalytic water oxidation performance.

A chronocoulometry experiment using an O_2 probe has also been performed with meso-$LiCoO_2$-I and meso-$LiCoO_2$-II to investigate the faradaic efficiency. The perfect agreement between the theoretical quantity of O_2 obtained from the number of coulombs and the experimental one obtained by O_2 probe indicates that the only origin of current density is catalytic water oxidation to O_2 evolution process and there are no competing redox reactions, see Figure S15 (Supporting Information).

3. Conclusion

Molten salt assisted self-assembly is an important assembly process that can be used for the synthesis of mesoporous metal lithiates. Both surfactants, nonionic and charged, are necessary in the assembly process in which the nonionic surfactants (oligo(ethylene oxide) type surfactants and pluronics) form the LLC mesophases with many salts and the charged surfactants accommodate and stabilize sufficient salts in the mesophase. Salts and ethanol or water are the nonvolatile and volatile solvents, respectively, in the process in which the volatile solvent (ethanol or water) assists in the assembly and thin film formations, where the salts are not only the precursors for the targeted oxides but they also stabilize the mesophase for further heat treatments.

Both lithium nitrate and cobalt nitrate and lithium nitrate and manganese nitrate salts form stable LLC mesophases in the presence of as high as 16 and 12 total salts/$C_{12}E_{10}$ mole rations, respectively, in the presence of 1:1 $C_{12}E_{10}$:CTAB ratios. The presence of CTAB in the $C_{12}E_{10}$ system, the Br-ion enforces the formation of $(CTA)_2[MBr_4]$ (M = Co(II) and Mn(II)) crystals that cause the formation of some oxide impurities in the Co(II) system. However, the formation of $(CTA)_2[MnBr_4]$ does not seem problematic. Moreover, the $(CTA)_2[MBr_4]$ formation dominates if the process is initiated in an aqueous media. The likely reason is that its solubility in ethanol is much higher therefore ethanol solutions can be used as the volatile solvent in the process.

Calcination of the mesophase produces meso-$LiCoO_2$ with some CoO, Co_3O_4, and $CoBr_2$ nanocrystallite impurities, which can be minimized when the CTAB is replaced with CTAN. The CTAN hinders the formation of any insoluble charge surfactant complex salt. Calcined films have characteristic disordered sponge like pore systems with highly crystalline pore-walls. The surface area of the $LiMn_2O_4$ system is slightly larger than that of $LiCoO_2$. The meso-$LiCoO_2$, coated over fluorine doped tin oxide (FTO), performs well as an electrode for water oxidation with the lowest overpotential (as low as 282 and 376 mV at 1 and 10 mA in a pH 14) recorded in the literature among the other $LiCoO_2$ systems. Further optimization of the synthesis conditions could improve these values and film qualities.

4. Experimental Section

General Method: Two salts ($LiNO_3.xH_2O$ and $[Co(H_2O)_6](NO_3)_2$ or $LiNO_3.xH_2O$ and $[Mn(H_2O)_4](NO_3)_2$, two surfactants (an ionic surfactant CTAB, $C_{16}H_{33}N(CH_3)_3Br$, and a nonionic surfactant, $C_{12}E_{10}$, $C_{12}H_{25}(OCH_2CH_2)OH$), HNO_3, and ethanol (or H_2O) as a volatile solvent were mixed in vials and homogenized for 12 h by stirring with a magnetic stirrer, to form clear solutions. The clear solutions were then spin coated over glass substrates to form LLC films. Finally, the LLC films were calcined at temperatures ranging from 300 to 700 °C in air. The amount of salt in the mesophase and final product, amount of acid, and the solvent type were optimized by preparing the clear solutions as described above. The solutions were then spin coated and calcined at the desired temperature to produce the final products.

The Optimization of Salt Amount: Seven homogenized solutions containing 0.8 mmol $C_{12}E_{10}$, 0.8 mmol CTAB, 6 g of ethanol with different amounts of salts were prepared with salts(Li(I) + Co(II))/$C_{12}E_{10}$ mole ratios of 4.5, 6, 9, 12, 15, 16, and 17. The films were prepared by spin coating above solutions over glass substrates at 1500 rpm for 7 s.

Determination of Solvents (Water vs Ethanol): The general method was performed using 6 g ethanol or 6 g water as the volatile solvent using 9 salts/surfactant mole ratio. Both sets were prepared (each set consists of 60–80 glass slides) by spin coating on glass substrates at 1500 rpm for 7 s, then calcined at 300 °C for 3 h.

Preparation of Meso-$LiCoO_2$ with/without CTAB: By employing the general method, two sets of samples were prepared with a total salt/surfactant mole ratio of 4.5, 6, and 9 with CTAB/$C_{12}E_{10}$ mole ratios of 0.0 and 1.0 by spin coating at 1500 rpm for 7 s (six sets of glass slides, each set consists of 60–80 slides). The samples were then calcined at 450 °C for 1 h and collected by scraping the slides. The high angle XRD patterns and N_2 sorption isotherms of the powders have been collected.

Preparation of Meso-$LiCoO_2$ Films Using $CoBr_2$ as the Cobalt Source: Two solutions were prepared using a salt/surfactant mole ratio of 9; one with a 4.5 mole ratio of cobalt nitrate hexahydrate and the other with 2 mole ratio of cobalt bromide and 2.5 mole ratio of cobalt nitrate salts using 0.8 mmol $C_{12}E_{10}$ and 0.8 mmol CTAB in 6 g of ethanol. Two sets (each set consists of 60–80 slides) of samples were prepared by spin coating the above solutions on glass substrates at 1500 rpm for 7 s and then calcined at 450 °C for 3 h. The powder samples were collected by scraping the slides.

Synthesis of CTAN ($C_{16}H_{33}N(CH_3)_3NO_3$): CTAN was synthesized by following a method described in the literature.[55] Briefly, $AgNO_3$ methanol–water (1:1 ratio) solution was prepared in dark by using 9.157 g $AgNO_3$, 100 g methanol and 100 g distilled water. A solution of CTAB, prepared by dissolving 20 g of CTAB in 100 g of methanol was added slowly to the above mixture by stirring in dark and stored in the dark for 10 d at low temperature (+4 °C). The solution was filtered with a Millipore TM system with a pore diameter of 1 µm to remove the AgBr particles. The methanol and water were then evaporated using a rotating evaporator and a vacuum oven. The resulting product was dissolved in methanol and recrystallized two times.

Preparation of Meso-$LiCoO_2$ Thin Films Using CTAN: A homogenized solution, containing 3.6 mmol $LiNO_3.xH_2O$, 3.6 mmol $[Co(H_2O)_6](NO_3)_2$, 0.8 mmol $C_{12}E_{10}$, and 0.8 mmol CTAN, and 6 g of ethanol, was prepared using the general method. A set of slides (around 80 slides) were then coated at 1500 rpm for 7 s and finally calcined at 450 °C for 10 h in air. The powder samples were obtained by scraping the slides for use in XRD and N_2 sorption measurements.

Preparation of $LiMn_2O_4$: The above parameters and procedures were used to prepare the solution, LLC thin films, and mesoporous $LiMn_2O_4$ thin films.

TEM Analysis: A homogenized solution of the required sample was spin coated over a glass substrate at 6000 rpm for 10 s to obtain a very thin film. The film was then calcined at the optimal temperature and duration, scraped from the substrate and ground in a mortar for 10 min to obtain smaller particles. The sample was then placed in a solution of ethanol and sonicated for 2 h to disperse the particles. The dispersed mixture was dropped on a carbon coated Cu grid with 300 mesh under a UV lamp. The dried grid was placed into TEM of JEOL JEM 2100 F operating at a voltage of 200 kV for imaging.

XRD Measurements: Thin film and powder XRD patterns were recorded by using a Rigaku Miniflex diffractometer, equipped with a Miniflex goniometer and an X-ray source with Cu $K\alpha$ radiation (λ = 1.5405 Å) operated at 30 kV and 15 mA. XRD patterns of the thin films were collected between 1° and 4° with a scan rate of 0.5° min^{-1}. The powder samples were packed into standard glass sample holders and the patterns were collected between 10° and 80°, 2θ, values with a scan rate of 0.5° min^{-1}. The diffraction patterns were indexed using the Joint Committee on Powder Diffraction Standards (JCPDS) cards.

N_2 (77.4 K) Sorption Measurements: Prior to measuring, the samples were dehydrated at 573 K for 2 h in vacuum. The N_2 sorption isotherms were measured using a TriStar 3000 automated gas adsorption analyzer (micrometrics) over a relative pressure range, P/P_0, from 0.01 to 0.99. The saturated pressure was measured over 120 min intervals. The surface areas of the different samples measured were calculated in the range of 0.05–0.30 relative pressure with 5 points.

POM Images: The POM images were recorded by using ZEISS Axio Scope.A1 polarizing optical microscope in transmittance mode from films, coated over glass slides.

FT-IR Measurements: The FT-IR spectra were recorded using a Bruker Tensor 27 model FT-IR spectrometer. A Digi Tect TM DLATGS detector was used with a resolution of 4.0 cm^{-1} from 400 to 4000 cm^{-1} range. The data obtained after 256 scans were recorded using films, coated over IR transparent silicon wafers.

Micro-Raman Measurements: LabRam confocal Raman microscope with a 300 mm focal length was used for the measurements. The device has a Ventus LP 532, 50 mW, diode pumped solid-state laser operator at 20–34 mW with a polarization ratio of 100:1, a wavelength of 532.1 nm, and a 1024 × 256 element CCD camera. The signal collected was transmitted via a fiber optic cable into the spectrometer with 600 g mm^{-1} grating. The Raman spectra of the samples were recorded by placing the probe tip on the desired point of the sample over the glass or silicon wafer.

Electrochemical Studies: A conventional three-electrode electrochemical cell was used with an Ag/AgCl electrode (3.5 M KCl) as the reference electrode, Pt wire as counter electrode, and catalyst modified FTO substrate as the working electrode. The neutral buffer solutions were prepared using K_2HPO_4 and KH_2PO_4 (KPi) and then adjusted by adding H_3PO_4 or 1 M KOH. A 1 M KOH solution was used for alkaline conditions (pH 14). CV were recorded with a scan rate of 100 mV s^{-1} in 50×10^{-3} M KPi (pH 7) containing 1 M KNO_3 as electrolyte between 0 and 1.5 V (vs Ag/AgCl) and all potentials displayed in the manuscript are iR-corrected. All experiments were carried out under nitrogen atmosphere. pH of the solution was measured by Mettler Toledo pH meter (S220). YSI 5100 dissolved oxygen sensing electrode instrument equipped with a dissolved oxygen field probe was used to determine the oxygen evolution.

Supporting Information

Supporting Information is available from the Wiley Online Library or from the author.

Acknowledgements

The authors thank the Scientific and Technological Research Council of Turkey (TÜBİTAK) under project number 113Z730 for financial support. Ö.D. is a member of Science Academy, Istanbul.

Conflict of Interest

The authors declare no conflict of interest.

Keywords

electrocatalysis, mesoporous thin films, metal lithiates, molten salt assisted self-assembly, water oxidation

Received: June 7, 2017
Revised: August 26, 2017
Published online: November 17, 2017

[1] N. Linares, A. M. Silvestre-Albero, E. Serrano, J. Silvestre-Albero, J. G. Garcia-Martinez, *Chem. Soc. Rev.* **2014**, *43*, 7681.
[2] M. S. Park, J. Kim, K. J. Kim, J. W. Lee, J. H. Kim, Y. Yamauchi, *Phys. Chem. Chem. Phys.* **2015**, *17*, 30963.
[3] G. Wang, H. Liu, J. Horvat, B. Wang, S. Qiao, J. Park, H. Ahn, *Chem. Eur. J.* **2010**, *16*, 11020.
[4] G. Gardner, J. Al-Sharab, N. Danilovic, Y. B. Go, K. Ayers, M. Greenblatt, G. C. Dismukes, *Energy Environ. Sci.* **2016**, *9*, 184.
[5] J. Wang, L. Li, H. Tian, Y. Zhang, X. Che, G. Li, *ACS Appl. Mater. Interfaces* **2017**, *9*, 7100.

[6] P. Yang, D. Zhao, D. I. Margolese, B. F. Chmelka, G. D. Stucky, *Chem. Mater.* **1999**, *11*, 2813.
[7] G. J. A. A. Soler-Illia, C. Sanchez, B. Lebeau, J. Patarin, *Chem. Rev.* **2002**, *102*, 4093.
[8] D. Grosso, G. J. A. A. Soler-Illia, E. L. Crepaldi, B. Charleux, C. Sanchez, *Adv. Funct. Mater.* **2003**, *13*, 37.
[9] D. Grosso, C. Boissière, B. Smarsly, T. Brezesinski, N. Pinna, P. A. Albouy, H. Amenitsch, M. Antonietti, C. Sanchez, *Nat. Mater.* **2004**, *3*, 787.
[10] Y. Ren, Z. Ma, P. G. Bruce, *Chem. Soc. Rev.* **2012**, *41*, 4909.
[11] G. J. A. A. Soler-Illia, O. Azzaroni, *Chem. Soc. Rev.* **2011**, *40*, 1107.
[12] N. D. Petkovich, A. Stein, R. A. Caruso, *Chem. Soc. Rev.* **2013**, *42*, 3721.
[13] F. Jiao, J. C. Jumas, M. Womes, A. V. Chadwick, A. Harrison, P. G. Bruce, *J. Am. Chem. Soc.* **2006**, *128*, 12905.
[14] K. Zhu, B. Yue, W. Zhou, H. He, *Chem. Commun.* **2003**, 98.
[15] B. Yue, H. Tang, Z. Kong, K. Zhu, C. Dickinson, W. Zhou, H. He, *Chem. Phys. Lett.* **2005**, *407*, 83.
[16] A. Rumplecker, F. Kleitz, E. L. Salabas, F. Schüth, *Chem. Mater.* **2007**, *19*, 485.
[17] F. Jiao, A. Harrison, A. H. Hill, P. G. Bruce, *Adv. Mater.* **2007**, *19*, 4063.
[18] H. Tüysüz, Y. Liu, C. Weidenthaler, F. Schüth, *J. Am. Chem. Soc.* **2008**, *130*, 14108.
[19] F. Jiao, A. Harrison, J. C. Jumas, A. W. Chadwick, W. K. Kockelmann, P. G. Bruce, *J. Am. Chem. Soc.* **2006**, *128*, 5468.
[20] H. J. Shin, R. Ryoo, Z. Liu, O. Terasaki, *J. Am. Chem. Soc.* **2001**, *123*, 1246.
[21] Y. Yamauchi, K. Kuroda, *Chem. Asian J.* **2008**, *3*, 664.
[22] C. Li, Ö. Dag, T. D. Dao, T. Nagao, Y. Sakarmoto, T. Kimura, O. Terasaki, Y. Yamauchi, *Nat. Commun.* **2015**, *6*, 6608.
[23] C. Li, B. Jiang, Z. Wang, Y. Li, M. S. A. Hossain, J. H. Kim, T. Takei, J. Henzie, Ö. Dag, Y. Bando, Y. Yamauchi, *Angew. Chem., Int. Ed.* **2016**, *55*, 12746.
[24] Y. Li, C. Li, B. P. Bastakoti, J. Tang, B. Jiang, J. Kim, M. Shababuddin, Y. Bando, J. H. Kim, Y. Yamauchi, *J. Mater. Chem. A* **2016**, *4*, 9169.
[25] D. M. Antonelli, J. Y. Ying, *Angew. Chem., Int. Ed.* **1995**, *34*, 2014.
[26] P. Yang, D. Zhao, D. I. Margolese, F. Bradley, B. F. Chemalka, G. D. Stucky, *Nature* **1998**, *396*, 152.
[27] P. Yang, D. Zhao, D. I. Margolese, F. Bradley, B. F. Chemalka, G. D. Stucky, *Chem. Mater.* **1999**, *11*, 2813.
[28] F. Schüth, *Chem. Mater.* **2001**, *13*, 3184.
[29] S. Y. Choi, M. Mamak, N. Coombs, N. Chopra, G. A. Ozin, *Adv. Funct. Mater.* **2004**, *14*, 335.
[30] S. W. Boettcher, J. Fan, C. K. Tsung, Q. Shi, G. D. Stucky, *Acc. Chem. Res.* **2007**, *40*, 784.
[31] F. Jiao, K. M. Shaju, P. G. Bruce, *Angew. Chem., Int. Ed.* **2005**, *44*, 6550.
[32] L. Luo, Y. Wang, H. Xiong, Y. Xia, *Chem. Mater.* **2007**, *19*, 4791.
[33] F. Jiao, J. Bao, A. H. Hill, P. G. Bruce, *Angew. Chem., Int. Ed.* **2008**, *47*, 9711.
[34] B. M. Hwang, S. J. Kim, Y. W. Lee, B. Han, S. B. Kim, W. S. Kim, K. W. Park, *Int. J. Electrochem. Sci.* **2013**, *8*, 9449.
[35] S. Chen, Z. Chen, C. Cao, *Electrochim. Acta* **2016**, *199*, 51.
[36] Y. Ren, A. R. Armstrong, F. Jiao, P. G. Bruce, *J. Am. Chem. Soc.* **2010**, *132*, 996.
[37] H. Liu, G. Wang, J. Liu, S. Qiao, A. Ahn, *J. Mater. Chem.* **2011**, *21*, 3046.
[38] C. Karakaya, Y. Türker, C. Albayrak, Ö. Dag, *Chem. Mater.* **2011**, *23*, 3062.
[39] C. Karakaya, Y. Türker, Ö. Dag, *Adv. Funct. Mater.* **2013**, *23*, 4002.
[40] C. Avcı, A. Aydın, Z. Tuna, Z. Yavuz, Y. Yamauchi, N. Suzuki, Ö. Dag, *Chem. Mater.* **2014**, *26*, 6050.
[41] F. M. Balcı, O. U. Kudu, E. Yılmaz, Ö. Dag, *Chem. Eur. J.* **2016**, *22*, 18873.
[42] Ö. Çelik, Ö. Dag, *Angew. Chem., Int. Ed.* **2001**, *40*, 3800.
[43] C. Albayrak, A. M. Soylu, Ö. Dag, *Langmuir* **2008**, *24*, 10592.
[44] C. Albayrak, A. Cihaner, Ö. Dag, *Chem. Eur. J.* **2012**, *18*, 4190.
[45] C. Albayrak, N. Özkan, Ö. Dag, *Langmuir* **2011**, *27*, 870.
[46] W. Huang, R. Frech, *Solid State Ion.* **1996**, *86–88*, 395.
[47] H. Porthault, R. B. Hadjean, F. Le Cras, C. Bourbon, S. Franger, *Vib. Spectrosc.* **2012**, *62*, 152.
[48] R. B. Hadjean, J. P. Pereira-Ramos, *Chem. Rev.* **2010**, *110*, 1278.
[49] D. A. Fine, *J. Am. Chem. Soc.* **1962**, *84*, 1139.
[50] S. J. Hwang, D. H. Park, J. H. Choy, G. Campet, *J. Phys. Chem. B* **2004**, *108*, 12713.
[51] G. Gardner, J. Al-Sharab, N. Danilovic, Y. B. Go, K. Ayers, M. Greenblatta, G. C. Dismukes, *Energy Environ. Sci.* **2016**, *9*, 184.
[52] Z. Lu, H. Wang, D. Kong, K. Yan, P.-C. Hsu, G. Zheng, H. Yao, Z. Liang, X. Sun, Y. Cui, *Nat. Commun.* **2014**, *5*, 4345.
[53] Z. Lu, G. Chen, Y. Li, H. Wang, J. Xie, L. Liao, C. Liu, Y. Liu, T. Wu, Y. Li, A. C. Luntz, M. Bajdich, Y. Cui, *J. Am. Chem. Soc.* **2017**, *139*, 6270.
[54] A. J. Esswein, M. J. McMurdo, P. N. Ross, A. T. Bell, T. D. Tilley, *J. Phys. Chem. C* **2009**, *113*, 15068.
[55] M. L. T. Liveri, R. Lombardo, C. Sbriziolo, G. Viscardi, P. Quagliotto, *New J. Chem.* **2004**, *28*, 793.